RSC Advances

PAPER

View Article Online
View Journal | View Issue

Cite this: *RSC Adv.*, 2015, **5**, 68143

Optical properties of thin metal films with nanohole arrays on porous alumina–aluminum structures

Juris Prikulis,*[a] Tomas Tamulevičius,[a] Raimonds Poplausks,[a] Gatis Bergs,[a] Indra Apsite,[a] Uldis Malinovskis,[a] Andris Actins[b] and Donats Erts[a]

Received 2nd July 2015
Accepted 30th July 2015

DOI: 10.1039/c5ra12880c

www.rsc.org/advances

A multilayer system is formed by the deposition of a 10–35 nm thin Au or Ag film with 18–25 nm diameter holes on 75–280 nm thick layers of porous anodized aluminum oxide (AAO) supported by a bulk sheet of aluminum. We present a detailed study of system parameters, which influence the optical response, including the porosity, metal layer thickness and crystallographic orientation of the Al substrate. The spectral properties are mainly governed by the interference of the reflections from the Al substrate and the thin metal film separated by the AAO layer. An enhanced plasmonic attenuation component near 650 nm for the Au films with holes can be observed when the interferometric anti-reflection condition is fulfilled close to this particular wavelength.

1 Introduction

Porous anodized aluminum oxide (AAO) is a well-known self-organized material,[1–3] which can be used as a template for the development of nanostructures[4] for applications in biotechnology,[5] semiconductor devices[6] and other fields of science. Recently, metal-coated AAO layers have attracted interest due to strong interference effects, which can be used for color filtering[7–9] or sensor applications.[10,11]

The spectral response of a metal–AAO–Al multilayer structure is mainly governed by the interference of light partly reflected and partly transmitted at the thin metal film and nearly ideally reflected from the Al surface. A model based on the optical path difference is often used for an explanation of the coloring of thin AAO layers[7,8,12–15] and provides a relationship between the wavelengths of reflection maxima and the AAO thickness.

However, at the microscopic level the layer interfaces are not flat. The optical properties change rapidly depending on the size of sub-wavelength features, such as the pore diameter.[8,10,16] Nanometer holes are formed during metal deposition on porous AAO and affect the reflection from metals.[3] Holes in metal films support plasmon modes[17] and may cause interesting effects, such as extraordinary optical transmission (EOT).[18] The use of an Au–AAO–Al system with ≈30 nm diameter holes in the Au film has been demonstrated in surface enhanced Raman scattering (SERS) experiments.[19] Furthermore, one can expect that due to propagating plasmon modes in the metal film, the optical properties in metal–AAO–Al systems may change depending on the pore ordering,[20] which varies depending on the anodization voltage during AAO synthesis.[21]

In this work we study the optical reflection from a metal–AAO–Al multilayer system depending on the AAO layer thickness and the morphology obtained using anodization in sulfuric and oxalic acids. We analyze the line shape of the reflection attenuation peaks and find absorption components outside the regular interferometric pattern. Absorption maxima at certain wavelengths emerge from the reflection spectra, when conditions near destructive interference are met. Furthermore, we study how the optical properties are affected by material choice (Ag or Au), the metal layer thickness, the crystallographic orientation of Al substrate, the illumination angle and polarization.

Nanohole arrays in metal films have been extensively studied during the past two decades[3,17–20,22–26] with much attention devoted to EOT in periodic structures.[27] Nanohole array production techniques include focused ion beam milling (FIB), imprinting, electron beam and nanosphere lithography.[28] High aspect ratio nanohole arrays have been produced by replication of the AAO pore structure.[29] Nanoholes with diameters in the range of 20 nm, of interest in the present study, are considerably smaller and their array packing is more dense than what is typically achieved using the mentioned production methods.

Potential applications of the presented multilayer structures include sensing[30] and the enhancement of fluorescence experiments.[23,26] An important advantage for the practical applications of hole arrays used in the present study is that their synthesis is a physicochemical process, which allows the production of large samples much faster and at a lower cost compared to lithography or FIB.

[a]*Institute of Chemical Physics, University of Latvia, 19 Raina Blvd., Riga LV-1586, Latvia. E-mail: juris.prikulis@lu.lv; Fax: +371 6703 3874; Tel: +371 6703 3875*
[b]*Faculty of Chemistry, University of Latvia, Riga, Latvia*

2 Methods and experiments

For the synthesis of AAO we follow a recipe described in detail elsewhere.[21] In brief, high purity aluminum foil (99.999%, Goodfellow, Cambridge) was degreased in acetone and annealed at 450 °C under vacuum for one hour and then slowly (20 °C h^{-1}) cooled to room temperature. The annealed aluminum sheets were electropolished under a constant voltage of 10 V at a temperature of 0 °C in a solution of perchloric acid (60% $HClO_4$) and ethanol (96% EtOH) in a volume ratio of 1 : 4.

Anodization was done using two different electrolyte solutions, which produce different pore diameters and separations. One series of samples was obtained by a two stage anodization at room temperature in 0.3 M sulfuric acid using a constant 20 V voltage in a two-electrode electrochemical cell with platinum cathode. The oxide layer after the first anodization stage was removed by a solution of CrO_3 and H_3PO_4 (4% : 11%) at 70 °C for 2 h. By selecting the duration of the second anodization as 30, 50, 70, 90 and 110 s, respective AAO layer thicknesses of 75, 120, 185, 225 and 250 nm were achieved. For the sulfuric acid electrolyte samples, pore widening was done in 5% H_3PO_4 for 1 min. The mean pore center separation for this type of samples was ≈ 50 nm and the pore diameter ≈ 20 nm. The other series of samples was produced using a 0.3 M oxalic acid electrolyte with a 40 V anodizing voltage. In this case, the pore center separation was ≈ 120 nm and the pore diameter ≈ 50 nm. The second anodization times for one particular set obtained using oxalic acid were 60, 120, 180, 240 and 300 s, which resulted in AAO thicknesses of 130, 160, 180, 230, 260 and 280 nm.

For most samples, a 20 nm thick Au layer was deposited on AAO using an ion beam-based GATAN Precision Etching and Coating System (model 682 PECS). The exceptions were the samples produced using a 20 nm layer of Ag and samples with a varying thickness (10–35 nm) of Au.

The sample pore diameter, separation, and AAO membrane thickness were determined from scanning electron microscope (SEM, Hitachi 4800) images (Fig. 1a and c) using ImageJ software.[31] The membrane thickness was obtained by averaging multiple measurements within the same sample, which vary in ±10–15 nm limits. For selected samples the layer thickness and porosity were also confirmed using a rotating compensator spectroscopic ellipsometer GES5-E (Semilab) with an automated goniometric bench and a CCD based detector in the 190–900 nm spectral range. Measurements were obtained at multiple points employing micro spot optics (theoretical spot size 365 × 470 μm at 75° on the sample). The refractive index and extinction dispersion curves, as well as the AAO void ratios and thicknesses, were obtained with Spectroscopic Ellipsometry Analyzer software (SEA, Semilab).

In the case of a large AAO layer thickness to pore diameter aspect ratio, *i.e.*, deep and narrow pores, the sputtered metal does not fill the pore volume, nor does it accumulate as nanoparticles at the bottom of the pores, but rather, it forms a film with holes on top of the membrane (Fig. 1b). The hole formation and emptiness of the AAO pores is confirmed by SEM measurements (Fig. 1c), however, the shape of holes is not perfectly cylindrical. The step coverage at the pore entrance results in a smaller concentration of voids in the metal layer. There is also a considerable roughness in the metal film due to the topography of the AAO surface.[32] This may cause some diffuse reflections and the broadening of spectral features.

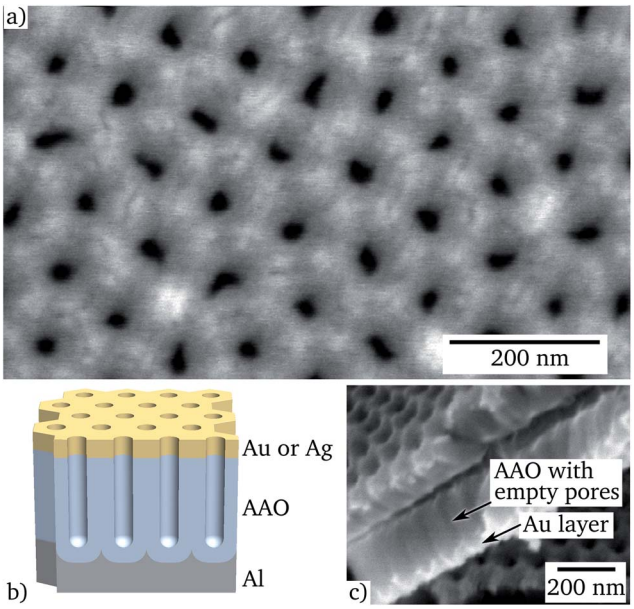

Fig. 1 Structure of metal–AAO–Al systems, (a) top view SEM image of a typical 20 nm Au layer deposited on AAO, which was obtained using oxalic acid electrolyte, (b) schematic diagram, and (c) a fractured sample surface showing the cross section of AAO with a thin Au layer.

Optical reflection spectra were measured using a spectrometer (Ocean Optics USB4000), which was connected to a microscope (Olympus IX71) with a 10× objective lens (Olympus CPLNFLN 10XPH, NA = 0.3) and a standard microscope halogen lamp. The reflection from electropolished aluminum foil without an AAO membrane was used as a reference to compensate for the spectral properties of the light source and detection system.

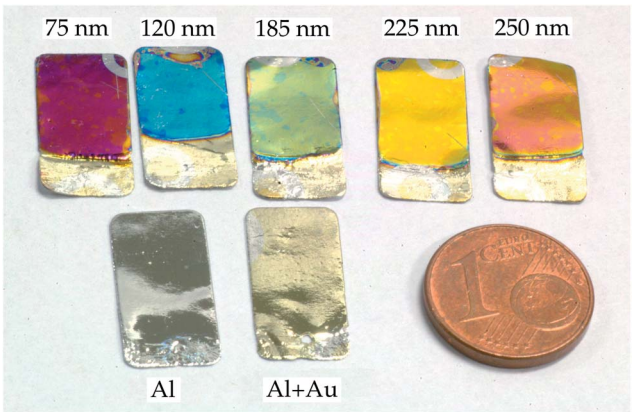

Fig. 2 Photograph of the series of samples with various AAO thicknesses prepared using sulfuric acid, the electropolished Al reference and a 20 nm Ag film on the Al substrate.

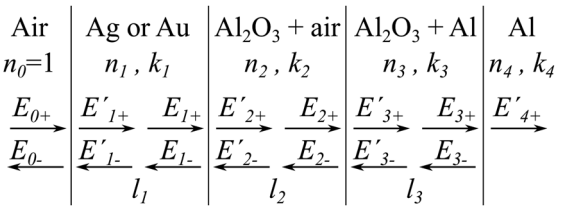

Fig. 3 Layer structure for the model calculations. The arrows indicate the direction of propagation for each wave component. The complex valued electric field amplitudes $E^{(\prime)}_{m(+/-)}$ with m = 0, 1,..., 4 at each interface are related through Fresnel equations.

Table 1 Sample parameters for the simulated spectra

Acid	% Void in l_1	l_1, nm	% Void in l_2	% Al in l_3	l_3, nm
Sulfuric	9	20	12	20	10
Oxalic	15	20	20	20	10

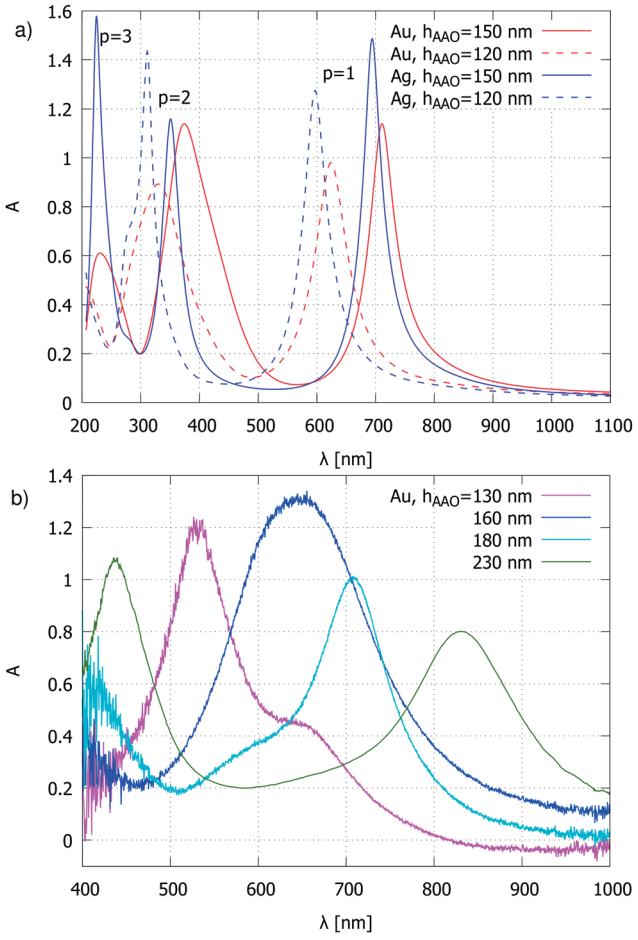

Fig. 4 (a) Calculated normal incidence reflection attenuation spectra for Au and Ag layers on AAO/Al with a parameter set, which corresponds to anodization in oxalic acid. (b) Measured spectra for 20 nm Au on oxalic-AAO layers of various thicknesses using an NA = 0.3 objective lens.

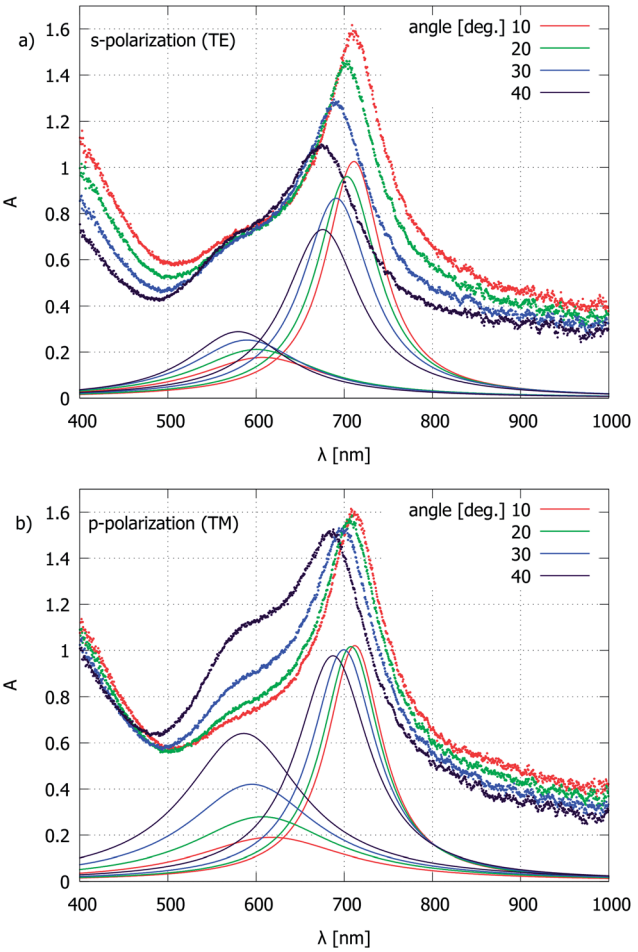

Fig. 5 Reflection attenuation spectra for a 180 nm oxalic-AAO sample coated with 20 nm of Au at different angles and polarizations of incidence radiation. The continuous lines show the Lorentzian fit of the p = 1 AR component centered near 700 nm and an extra attenuation component near 600 nm.

For angle-dependent spectral measurements at different polarizations, a custom-built reflectance measurement stand was used.[33] It consisted of a light source (incandescent light bulb), collimating optics, a Glan–Taylor polarizer controlled by a motorized rotational stage and a motorized sample/detector goniometric stage (full step resolution 0.6 arcmin, Standa). The reflected light was coupled to the optical fiber *via* a quartz lens and the spectra were measured with a CCD spectrometer (Avantes).

The crystallographic properties were analyzed using X-ray diffraction (XRD) (Bruker D8 ADVANCE) with Cu K_α radiation of wavelength 1.54 Å and a position sensitive detector LynxEye. X'Pert HighScore software was used to process the XRD data.

The surface topology was analyzed using an atomic force microscope (Asylum Research MFP-3D) operated in AC mode in air using an Olympus AC160TS cantilever with resonant frequency ≈ 300 kHz and spring constant ≈ 42 N m^{-1}. The data was subsequently processed using Igor Pro software (WaveMetrics).

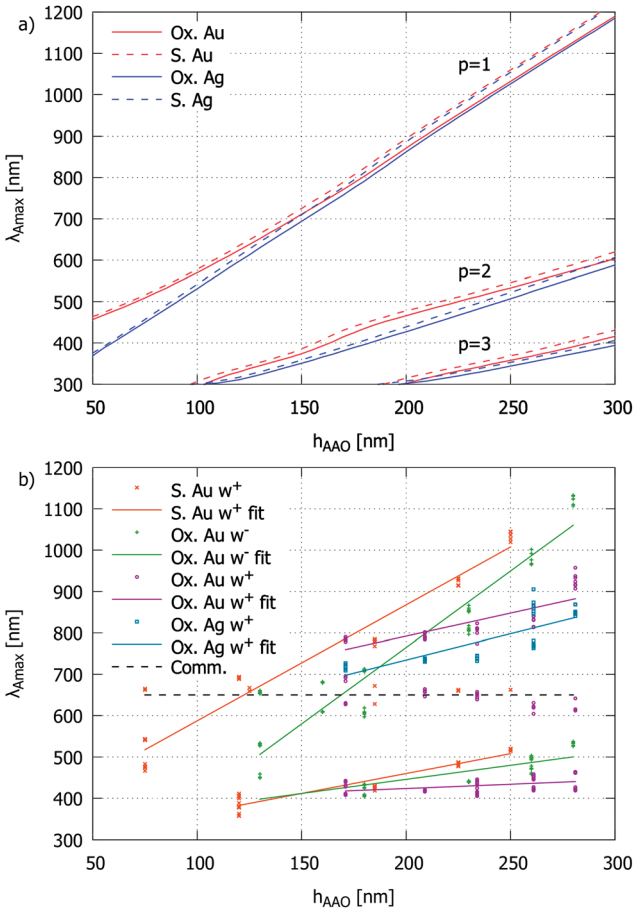

Fig. 6 Wavelength of the attenuation maxima depending on the AAO thickness for the Au–AAO–Al structures. "S." ("Ox.") indicates a sulfuric (oxalic) acid electrolyte solution. "w^{+}" and "w^{-}" indicate whether pore widening was done (superscript +) or not (superscript −). (a) Calculated with parameters from Table 1, and (b) measured reflection attenuation peaks. The black dashed line indicates the common plasmonic attenuation component observed for the Au-coated samples of a peak wavelength near 650 nm.

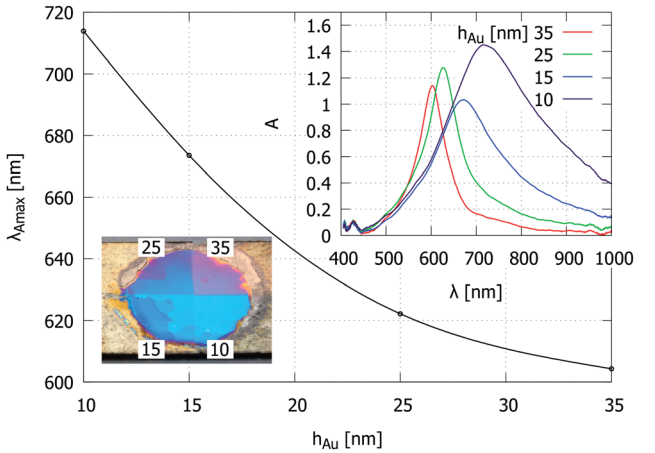

Fig. 7 Change in the reflection attenuation peak wavelength of an Au–AAO–Al sample, depending on the Au layer thickness. For this particular sample, $h_{AAO} = 125$ nm and pore widening was done before metal deposition. Insets: sample photograph and the spectra from regions with different Au thicknesses.

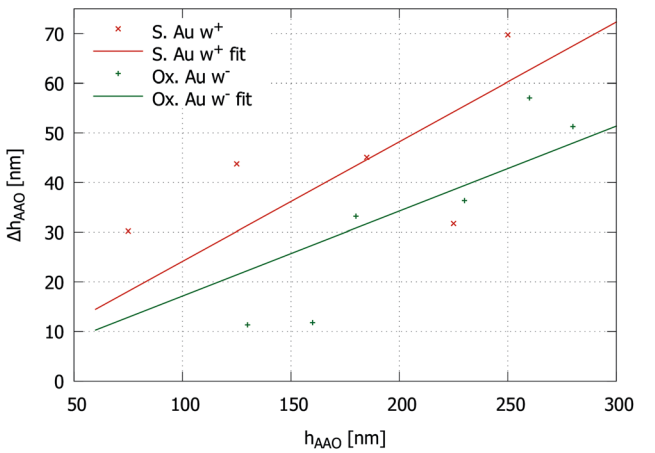

Fig. 8 AAO layer thickness variation due to the crystallographic domain structure in the Al substrate.

3 Results and discussion

3.1 Spectral properties

The obtained samples appear in bright and saturated colors to an unaided eye (Fig. 2). One can easily observe that the surface contains multiple grains, some of which are several hundred μm wide, of notably different colors due to variations in the AAO thickness, which we will address later. However, all samples have one particular dominant color tone, which we use for spectral analysis. For the characterization of the sample optical properties, we express the attenuation of reflection as:

$$A = -\log_{10}\left(\frac{I}{I_0}\right). \quad (1)$$

Here, I is the reflected intensity from the sample under investigation and I_0 is the intensity recorded from the electropolished Al reference.

For the simulation of the reflection spectra, we consider a multilayer system interfacing air ($n_0 = 1$), as shown in Fig. 3.

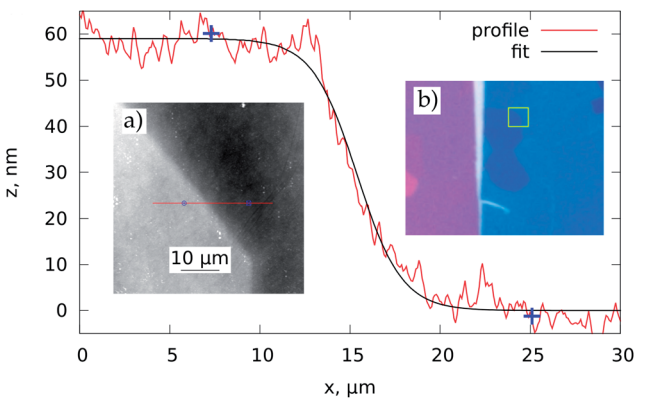

Fig. 9 Domain height profile. Insets: (a) AFM image; (b) optical image of the same area. The color differences are caused by different coatings of this particular sample: Ag (left, violet) and Au (right, blue).

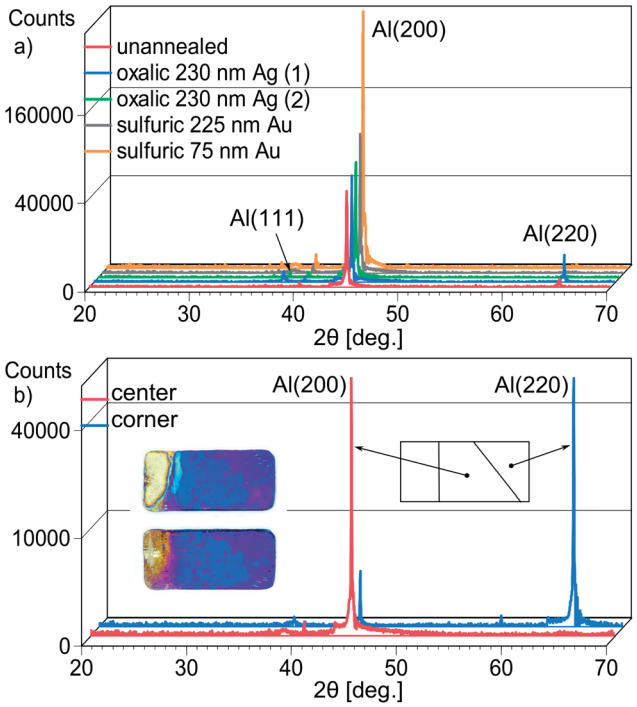

Fig. 10 X-ray diffractograms of (a) a representative selection of typical samples from different synthesis experiments and (b) selected sample areas with an inverted optical domain contrast. Inset: top and bottom (mirrored) photographs of the sample before cutting and XRD analysis.

Table 2 Sample parameters from spectroscopic ellipsometry. l_1, l_2, and l_3 denote the thickness of the metal, AAO, and transition layer from Al_2O_3 to bulk Al (Fig. 3). l_2^* represents Al_2O_3 pores filled with Au. "w^+" and "w^-" indicate pore widening, as in Fig. 6

Sample	Ox. Au w^-	S. Au w^+	S. Au w^-	S. Ag w^-
h_{AAO}, nm (SEM)	180	185	125	125
l_1, nm	20 ± 1	20 ± 1	20 ± 2	29 ± 2
% Void in l_1	48 ± 2	17 ± 2	16 ± 3	17 ± 3
l_2, nm	175 ± 3	182 ± 1	120 ± 6	117 ± 6
% Void in l_2	44 ± 13	22 ± 8	21 ± 16	7 ± 3
l_2^*, nm	6 ± 4	—	—	—
% Au in l_2^*	31 ± 26	—	—	—
n_{AAO} at 600 nm	1.43 ± 0.03	1.51 ± 0.02	1.61 ± 0.05	1.64 ± 0.05
l_3, nm	7 ± 2	27 ± 11	7 ± 2	6 ± 2
% Al in l_3	82 ± 13	34 ± 10	38 ± 26	70 ± 28

The first layer represents an Ag or Au film of thickness l_1, with a complex refractive index of $n_1 + ik_1$. Similarly, $l_2 = h_{AAO}$ and $n_2 + ik_2$ describe porous alumina. The transition from Al_2O_3 to bulk Al is characterized by a single layer[34] of thickness l_3 and a refractive index of $n_3 + ik_3$, although further division in sub-layers could improve the accuracy.[35] Finally, the bulk Al has a refractive index of $n_4 + ik_4$. Realistic nk values are calculated using the Bruggeman model,[11,34,36] with geometry estimates from the SEM measurements listed in Table 1. In order to highlight the effect of porosity, most parameters are deliberately kept constant, in particular the thickness of the transition layer from Al_2O_3 to Al, which would in practice change

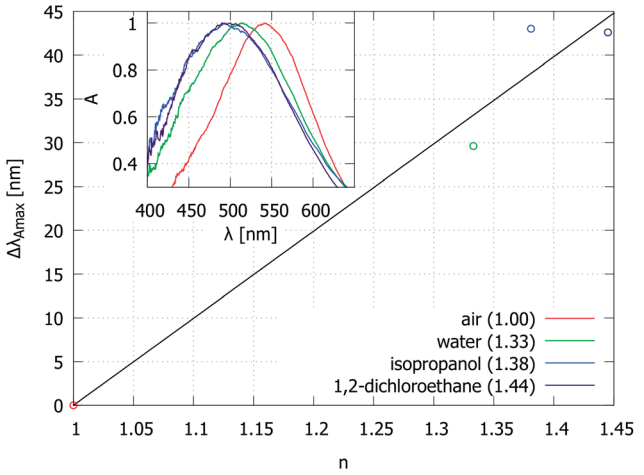

Fig. 11 Change of the reflection attenuation peak wavelength of an Au–AAO–Al (sulfuric acid, with pore widening, $h_{AAO} = 75$ nm) sample in various media. Inset: the normalized $p = 1$ spectra for peak detection.

depending on the anodisation voltage, electrolyte solution and pore widening time. Tabulated values for alumina[37] and all metals[38] were used to obtain the required dielectric functions.

For simplicity, we assume only normal incidence. For angle dependent reflections, one would need to take into account individual polarization components[39] and the anisotropy of the AAO layer.[36,40,41] The reflection attenuation from the entire system can be found by calculating the ratio of the electric fields E_{0-}/E_{0+} at the first surface $z_0 = 0$, using matching and propagation matrices.[42]

Each spectrum contains multiple attenuation maxima (Fig. 4a), which correspond to the destructive interference anti-reflection (AR) condition. They can be labeled $p = 1, 2, 3,\ldots$ starting from long wavelengths. For the calculated spectra in the red spectral region, where both Au and Ag are good reflectors, the attenuation peaks are well-separated symmetric line shapes, whereas in the violet-UV region, additional attenuation peaks appear due to absorption.

However, in the measured spectra for the Au layers (Fig. 4b), an additional component emerges when the interferometric attenuation maximum happens to be centered near 600–650 nm. This is best observed as a "shoulder" in the attenuation peaks for the samples with an AAO layer thickness of 130 and 180 nm, whereas for the 160 nm case, the two components overlap and produce a much broader peak width. Interestingly, the extra attenuation component becomes almost invisible for the 230 nm sample, when the $p = 1$ and $p = 2$ AR peaks are far away from 600–650 nm.

It should be noted that the spectra in Fig. 4b are recorded from an area of approximately 20 μm diameter within an angular aperture of $a/2 = 17.5°$ of the microscope objective lens, and are slightly blue-shifted relative to the reflection from purely normal incidence. This can be deduced from the measurements with collimated light, where a significant change in reflection attenuation is observed, depending on the angle of incidence and polarization (Fig. 5). In order to find the

maximum position of the individual components, a fit to a sum of Lorentzian line shapes is used. The wavelength shift of the $p = 1$ attenuation peak for an increase in the incidence angle is an expected behavior for the interferometric AR coating. The extra attenuation peak near 600 nm is of plasmonic nature, where both localized (LSP) and propagating (SPP) modes may be of importance.[43,44] The LSP mode can be identified by the extrapolation of the individual hole scattering peaks from the single-layer Au film measurements[22,24] to diameters in the 20 nm range, which would lead to maximum wavelength values near 600 nm. For high hole densities in disordered arrays, one would expect a blue-shift of the optical spectra;[22] however, as we shall see shortly, the plasmonic attenuation maximum wavelength for the present type of samples is insensitive to hole separation. This can be explained by the similarity between the optical properties of holes and particles and the fact that in the 20 nm diameter range, for Au, absorption dominates over scattering[45] and therefore the inter-particle or inter-hole interaction is weak. Another possibility is SPP launching by grating coupling, although the surface structure is not strictly periodic and contains a continuous spectrum of spatial frequencies. A more detailed electromagnetic simulation is required to find the angle dependence of various components. The different behavior of the 600 nm peak, and in particular, its height for *p*-polarized illumination (Fig. 5b) relative to the $p = 1$ attenuation component confirms that it is not related to the grain thickness variations of the AAO layer. The reflection spectra collected through the microscope are somewhat broadened due to the finite angular aperture of the objective lens; however, this setup allows us to address individual grains.

By comparing the plasmonic attenuation peak height at different angles and polarizations, one can estimate that at normal incidence the peak would be red-shifted and weakened but would not disappear completely. The amplitude change of this attenuation component depending on the AAO thickness (Fig. 4b) could be discussed in terms of Fano resonances,[46] since the system has both interferometric and resonant elements. The peculiar behavior can also be understood by considering the reflection from the Al surface, where the electric field forms a standing wave with the maximum amplitude at a certain distance ($\lambda/4$ condition plus a phase component due to the specific refractive index and thickness combination in a multilayer system) from the Al surface, *i.e.*, the interaction with holes in films can be maximized if the AAO layer fulfills the AR interference criterion. The effect can be further amplified by multiple Fabry–Pérot-like reflections. In comparison to periodic hole arrays with a significantly larger diameter and separation,[47–49] we do not observe as many narrow attenuation peaks within a comparable spectral range. While the shift of the $p = 1$ attenuation peak can be explained by a change of the optical path depending on the illumination angle, the origin of the plasmonic peak shift may be similar to the case of strictly periodic hole arrays.

In order to analyze the behavior of the different attenuation components, we plot their maximum wavelengths as a function of AAO layer thickness. Fig. 6a shows the calculated $p = 1$, 2, 3 AR peak positions from the multilayer model. Fig. 6b shows the peak positions obtained by a multiple Lorentzian fit to the experimental data. The continuous lines show linear fits to the $p = 1$, 2 peak positions, which were identified for the individual sample series where all of the synthesis parameters except the AAO layer thickness were kept constant. The multiple datapoints for the same average sample thickness represent spectra from different grains of the same dominant color tone. Despite this measurement uncertainty, there is a qualitative agreement with the simulation curves, namely, an increased porosity causes the blue-shift of reflection spectra, and a comparison between the two different metal (Au and Ag) coatings shows similar differences. The key observation is that for the Au-coated samples, there is a common plasmonic attenuation component near 650 nm (black dashed line) that is apparently invariant to changes in the pore separation, diameter, and AAO layer thickness. This behavior is different from the observations of nanohole arrays with larger hole diameters, where changes in the hole size and separation cause significant spectral shifts.[17,20,22,23,25] We also note that normally, this attenuation component is relatively weak and becomes obvious only near the AR condition (Fig. 4b), when the intensity is plotted on a logarithmic scale (eqn (1)). Further, the interferometric peak and the visibility of the extra attenuation component are modified by the metal layer thickness. This is demonstrated on a sample, which was divided into 4 segments and subjected to the deposition of different Au layers (Fig. 7). The absorption maximum shifts to shorter wavelengths and becomes narrower when the metal layer thickness is increased. This attenuation component would disappear for a larger metal layer thickness, approaching the reflection from the bulk material.

A limited number of samples were prepared, with one half coated with Ag and the other with Au, in order to demonstrate the effect of different metals. The $p = 1$ component for Ag appears at shorter wavelengths. However, other attenuation components appear in the UV-violet region, which suffers from a poor signal to noise ratio in the present setup.

3.2 Influence of the Al substrate

We now turn our attention to the grain structure, which can be observed in Fig. 2 and in some previous studies of metal–AAO–Al multilayer structures[7,8] but has not been analyzed in detail. The grains are caused by differences in the crystallographic orientation of domains in the Al sheet during sample production. Typically isolated grains appear blue-shifted relative to the dominant color tone, which means that their AAO layer thickness is thinner. By measuring the maximum difference of the $p = 1$ attenuation center wavelengths from individual grains (including the obviously different ones) within each sample, and the slope estimates $d\lambda_{Amax}/dh_{AAO}$ from Fig. 6b, one can obtain the AAO thickness variation due to granularity (Fig. 8). The obtained values are similar to the AAO thickness variation within $\pm$10–15 nm, as observed in the SEM measurements. The increasing thickness difference with an increase in the overall AAO thickness indicates that the anodization reaction occurs at different rates within each grain.

An analysis of the surface topology using AFM shows that a grain with a thinner AAO layer is actually higher relative to a neighboring grain with a larger thickness of the AAO layer (Fig. 9). Consequently, the chemical dissolution of Al in such grains is slower during electropolishing and anodic oxidation.

In order to determine which type of grains correspond to different AAO layer thicknesses, the samples were analyzed using XRD. The dominant crystallographic orientation for the majority of samples is (100) (Fig. 10a). An odd sample with a significant area of an inverted grain pattern was cut into pieces, and these areas were analyzed separately (Fig. 10b). It becomes evident that grains with thinner AAO layers have the (110) orientation. Similar results were obtained for thick AAO membranes exceeding 100 μm.[50] The preferred orientations arise during annealing,[51] however, we note that (220) grains occur near the sample edges and are likely seeded by mechanical stress when the Al sheets are cut prior to thermal treatment.

The (100) grains produce the best pore ordering,[50,52,53] however, the (110) grains have a smaller AAO layer thickness when produced at identical conditions. This affects the ordering of the resulting structure when the AAO membranes are transferred and used as contact masks for nanoparticle array production.[21] The thinner AAO layer above the (110) grains makes the deposited material penetrate more easily through pores. This mechanism causes the formation of high density disordered arrays.[54]

3.3 Material parameters

For the model calculations, dielectric functions were used based on geometry estimates from the SEM measurements and tabulated material data. For purposes of comparison, selected samples were analyzed using spectroscopic ellipsometry. In the case of AAO obtained using sulfuric acid, the layer structure of Fig. 3 was sufficient to fit the refractive index data, whereas for the oxalic type of samples, an extra layer of Au + Al_2O_3 with thickness l_2^* was needed. There is a variation in the obtained results within each sample, which is most likely due to the grain structure. The value ranges are summarized in Table 2. The SE measurements of the layer thickness agree well with the SEM estimates. The values generally follow the expected trends based on the calculated porosity, however, a considerable scatter is observed in the concentration data in various phases. It may be caused by some metal that exists on the pore walls and the accuracy of the model used for data fitting. The model also does not include the barrier layer, which certainly adds an extra optical path, but cannot be independently controlled during the synthesis process.

Finally, we demonstrate the variation of the reflection attenuation spectra when Au–AAO–Al systems are immersed in liquids with different refractive indexes (Fig. 11). There is a considerable scatter in the measured $d\lambda_{Amax}/dn$ data, which is likely caused by pore filling with air and sample heating. For sensor applications, one would need to develop a precise control of whether the liquid modifies the AAO pore refractive index, interacts with voids in the metal layer or changes the refractive index of the surrounding medium, n_0.

4 Conclusions

We have performed a survey of parameters which determine the reflection attenuation from a multilayer system consisting of thin metal films with nanohole arrays, porous AAO, and bulk Al. Apart from the thickness-dependent interference effects from reflections at various interfaces, we observe absorption components near 650 nm for the Au-coated samples, which can be attributed to the excitation of localized plasmons in holes in the metal film. This attenuation component is very weak in most cases and becomes obvious only when the interferometric anti-reflection wavelength is close to the absorption maximum. We presume that for this reason, the extra attenuation component has escaped unnoticed in previous studies of similar systems. Further development towards applications would be achieved through studies of how the interaction between the interferometric and plasmonic effects can be used for the enhancement of inelastic scattering.[19,23,26] Due to a nearly ideal reflection from the Al surface, a 4 times geometric gain can be reached.

Unlike in studies where AAO is synthesized on evaporated polycrystalline Al films,[36] the crystallographic domain structure of the Al substrate changes the chemical reaction rate, which alters the AAO thickness. By simple optical imaging, one can identify grains with (100) and (110) orientation, which might be of interest for further research[55] or the quality assessment of alloys.[56] The metal coating greatly increases the image contrast for such purposes. The thickness variations between the grains may be used to find optimal parameters for certain applications and provides regions with a distinct, well-defined set of parameters. The height variation between the different grains limits the size of uniform AAO membranes for use as deposition masks.

Finally, we have demonstrated the influence of metal choice, metal thickness and refractive index of the surrounding material on reflection spectra. These factors may be useful for colorimetric sensor applications.

Acknowledgements

This work was done within the ESF project 2013/0028/1DP/1.1.1.2.0/13/APIA/VIAA/054.

References

1 F. Keller, M. S. Hunter and D. L. Robinson, *J. Electrochem. Soc.*, 1953, **100**, 411.
2 J. P. O'Sullivan and G. C. Wood, *Proc. R. Soc. London, Ser. A*, 1970, **317**, 511–543.
3 H. Masuda and K. Fukuda, *Science*, 1995, **268**, 1466–1468.
4 J. C. Hulteen and C. R. Martin, *J. Mater. Chem.*, 1997, **7**, 1075–1087.
5 C. J. Ingham, J. ter Maat and W. M. de Vos, *Biotechnol. Adv.*, 2012, **30**, 1089–1099.
6 B. Polyakov, B. Daly, J. Prikulis, V. Lisauskas, B. Vengalis, M. A. A. Morris, J. D. Holmes and D. Erts, *Adv. Mater.*, 2006, **18**, 1812–1816.

7 X. Wang, H. Zhang, D. Zhang, Y. Ma, H.-J. Fecht and J. Z. Jiang, *Microsc. Res. Tech.*, 2012, **75**, 698–701.
8 J. Li, Z. Zhu, P. Deng, Y. Hu, J. Chu and W. Huang, *Proc. SPIE*, 2012, **8564**, 85640Q.
9 X. Hu, Z. Y. Ling, X. H. He and S. S. Chen, *J. Electrochem. Soc.*, 2009, **156**, C176.
10 T. Kumeria and D. Losic, *Nanoscale Res. Lett.*, 2012, **7**, 88.
11 L. P. Hernández-Eguía, J. Ferré-Borrull, G. Macias, J. Pallarès and L. F. Marsal, *Nanoscale Res. Lett.*, 2014, **9**, 414.
12 Y. Liu, H. Wang, J. Indacochea and M. Wang, *Sens. Actuators, B*, 2011, **160**, 1149–1158.
13 Q. Xu, Y. Yang, J. Gu, Z. Li and H. Sun, *Mater. Lett.*, 2012, **74**, 137–139.
14 K. Huang, Y. Li, Z. Wu, C. Li, H. Lai and J. Kang, *Opt. Express*, 2011, **19**, 1301–1309.
15 H. M. Chen, C. F. Hsin, R.-S. Liu, S.-F. Hu and C.-Y. Huang, *J. Electrochem. Soc.*, 2007, **154**, K11.
16 W. Xu, H. Chen, M. Zheng, G. Ding and W. Shen, *Opt. Mater.*, 2006, **28**, 1160–1165.
17 S.-H. Chang, S. Gray and G. Schatz, *Opt. Express*, 2005, **13**, 3150–3165.
18 T. Ebbesen, H. J. Lezec, H. F. Ghaemi, T. Thio and P. A. Wolff, *Nature*, 1998, **86**, 1114–1117.
19 D. Choi, Y. Choi, S. Hong, T. Kang and L. P. Lee, *Small*, 2010, **6**, 1741–1744.
20 F. Przybilla, C. Genet and T. W. Ebbesen, *Opt. Express*, 2012, **20**, 4697–4709.
21 U. Malinovskis, R. Poplausks, I. Apsite, R. Meija, J. Prikulis, F. Lombardi and D. Erts, *J. Phys. Chem. C*, 2014, **118**, 8685–8690.
22 J. Prikulis, P. Hanarp, L. Olofsson, D. Sutherland and M. Käll, *Nano Lett.*, 2004, **4**, 1003–1007.
23 A. G. Brolo, S. C. Kwok, M. G. Moffitt, R. Gordon, J. Riordon and K. L. Kavanagh, *J. Am. Chem. Soc.*, 2005, **127**, 14936–14941.
24 T. Rindzevicius, Y. Alaverdyan, B. Sepulveda, T. Pakizeh, M. Käll, R. Hillenbrand, J. Aizpurua and F. J. García de Abajo, *J. Phys. Chem. C*, 2007, **111**, 1207–1212.
25 L. Wu, P. Bai, X. Zhou and E. P. Li, *IEEE Photonics J.*, 2012, **4**, 26–33.
26 T. M. Schmidt, V. E. Bochenkov, J. D. A. Espinoza, E. C. P. Smits, A. M. Muzafarov, Y. N. Kononevich and D. S. Sutherland, *J. Phys. Chem. C*, 2014, **118**, 2138–2145.
27 F. J. Garcia-Vidal, L. Martin-Moreno, T. W. Ebbesen and L. Kuipers, *Rev. Mod. Phys.*, 2010, **82**, 729–787.
28 J.-F. Masson, M.-P. Murray-Méthot and L. S. Live, *Analyst*, 2010, **135**, 1483.
29 T. Yanagishita, K. Nishio and H. Masuda, *Adv. Mater.*, 2005, **17**, 2241–2243.
30 A. B. Dahlin, *Analyst*, 2015, **140**, 4748–4759.
31 C. A. Schneider, W. S. Rasband and K. W. Eliceiri, *Nat. Methods*, 2012, **9**, 671–675.
32 D. C. Leitao, J. Ventura, C. T. Sousa, J. M. Teixeira, J. B. Sousa, M. Jaafar, A. Asenjo, M. Vazquez, J. M. de Teresa and J. P. Araujo, *Nanotechnology*, 2012, **23**, 425701.
33 T. Tamulevicius, I. Gražuleviute, D. Urbonas, M. Gabalis, R. Petruškevicius and S. Tamulevicius, *Opt. Express*, 2014, **22**, 27462–27475.
34 J. de Laet, J. Vanhellemont, H. Terryn and J. Vereecken, *Appl. Phys. A: Solids Surf.*, 1992, **54**, 72–78.
35 N. Stein, M. Rommelfangen, V. Hody, L. Johann and J. M. Lecuire, *Electrochim. Acta*, 2002, **47**, 1811–1817.
36 A. C. Gâlcă, E. S. Kooij, H. Wormeester, C. Salm, V. Leca, J. H. Rector and B. Poelsema, *J. Appl. Phys.*, 2003, **94**, 4296.
37 I. H. Malitson and M. J. Dodge, *J. Opt. Soc. Am.*, 1972, **62**, 1405.
38 A. D. Rakic, A. B. Djurisic, J. M. Elazar and M. L. Majewski, *Appl. Opt.*, 1998, **37**, 5271–5283.
39 J. Lekner, *Theory of Reflection of Electromagnetic and Particle Waves*, Springer, 1987.
40 N. Lehman, R. Venkat and R. Schill, *J. Electrochem. Soc.*, 2009, **156**, C75.
41 Y. Jung, J. Byun, D. Woo and Y. Kim, *Thin Solid Films*, 2009, **517**, 3726–3730.
42 S. J. Orfanidis, *Electromagnetic Waves and Antennas*, Rutgers University, Piscataway, NJ, 2008.
43 T. A. Kelf, Y. Sugawara, R. M. Cole, J. J. Baumberg, M. E. Abdelsalam, S. Cintra, S. Mahajan, A. E. Russell and P. N. Bartlett, *Phys. Rev. B: Condens. Matter Mater. Phys.*, 2006, **74**, 245415.
44 L. S. Live, A. Dhawan, K. F. Gibson, H.-P. Poirier-Richard, D. Graham, M. Canva, T. Vo-Dinh and J.-F. Masson, *Anal. Bioanal. Chem.*, 2012, **404**, 2859–2868.
45 P. K. Jain, K. S. Lee, I. H. El-Sayed and M. A. El-Sayed, *J. Phys. Chem. B*, 2006, **110**, 7238–7248.
46 B. Luk'yanchuk, N. I. Zheludev, S. A. Maier, N. J. Halas, P. Nordlander, H. Giessen and C. T. Chong, *Nat. Mater.*, 2010, **9**, 707–715.
47 W. L. Barnes, W. a. Murray, J. Dintinger, E. Devaux and T. W. Ebbesen, *Phys. Rev. Lett.*, 2004, **92**, 107401.
48 H. Gao, W. Zhou and T. W. Odom, *Adv. Funct. Mater.*, 2010, **20**, 529–539.
49 M. Couture, Y. Liang, H.-P. Poirier Richard, R. Faid, W. Peng and J.-F. Masson, *Nanoscale*, 2013, **5**, 12399.
50 C. K. Y. Ng and A. H. W. Ngan, *Chem. Mater.*, 2011, **23**, 5264–5268.
51 F. Rashidi, T. Masuda, H. Asoh and S. Ono, *Surf. Interface Anal.*, 2013, **45**, 1490–1496.
52 G. Beck and K. Petrikowski, *Surf. Coat. Technol.*, 2008, **202**, 5084–5091.
53 C. Cheng, K. Y. Ng, N. R. Aluru and a. H. W. Ngan, *J. Appl. Phys.*, 2013, **113**, 204903.
54 J. Prikulis, U. Malinovskis, R. Poplausks, I. Apsite, G. Bergs and D. Erts, *Plasmonics*, 2014, **9**, 427–434.
55 V. V. Konovalov, G. Zangari and R. M. Metzger, *Chem. Mater.*, 1999, **11**, 1949–1951.
56 G. Beck and S. Funk, *Surf. Coat. Technol.*, 2012, **206**, 2371–2379.

